Discrete unified gas kinetic scheme for all Knudsen number flows: Low-speed isothermal case

Zhaoli Guo,[1,*] Kun Xu,[2,†] and Ruijie Wang[3,‡]
[1]*State Key Laboratory of Coal Combustion, Huazhong University of Science and Technology, Wuhan 430074, China*
[2]*Department of Mathematics, Hong Kong University of Science and Technology, Clear Water Bay, Hong Kong, China*
[3]*Nano Science and Technology Program, Hong Kong University of Science and Technology, Clear Water Bay, Hong Kong, China*
(Received 28 May 2013; revised manuscript received 13 August 2013; published 27 September 2013)

Based on the Boltzmann-BGK (Bhatnagar-Gross-Krook) equation, in this paper a discrete unified gas kinetic scheme (DUGKS) is developed for low-speed isothermal flows. The DUGKS is a finite-volume scheme with the discretization of particle velocity space. After the introduction of two auxiliary distribution functions with the inclusion of collision effect, the DUGKS becomes a fully explicit scheme for the update of distribution function. Furthermore, the scheme is an asymptotic preserving method, where the time step is only determined by the Courant-Friedricks-Lewy condition in the continuum limit. Numerical results demonstrate that accurate solutions in both continuum and rarefied flow regimes can be obtained from the current DUGKS. The comparison between the DUGKS and the well-defined lattice Boltzmann equation method (D2Q9) is presented as well.

DOI: 10.1103/PhysRevE.88.033305 PACS number(s): 47.11.St, 47.45.−n, 47.61.−k

I. INTRODUCTION

With the increasing demand in simulating multiscale fluid flows, numerical methods based on kinetic theory have attracted much attention. A variety of kinetic methods have been developed in recent years, such as the lattice gas automata method [1], the lattice Boltzmann equation (LBE) method [2], the gas kinetic scheme (GKS) method [3,4], and the dissipative particle dynamics method [5], among which the LBE and GKS methods are specifically designed for computational fluid dynamics (CFD). The kinetic nature of the LBE and GKS has led to many distinctive advantages that distinguish them from classical CFD methods, and a variety of successful applications in multiscale flows have been achieved [6–13].

Although sharing the common connection with the Boltzmann equation, the LBE and GKS methods exhibit some clear differences. First, the LBE is a finite-difference scheme with a discrete particle velocity set coupled with a regular lattice, while the GKS is a finite-volume formulation with a continuous particle velocity space. Second, the equilibrium distribution in LBE is an approximation to the Maxwellian distribution by its low-order expansion around zero velocity, and so the LBE is limited to nearly incompressible flows at low Mach number; on the other hand, the GKS uses a complete Maxwellian distribution as the equilibrium state and is therefore valid for fully compressible flow simulations. Third, the LBE solves the (nearly) incompressible Navier-Stokes equations implicitly through the proper choice of the discrete velocity set and the discrete equilibrium distribution functions, while the GKS solves the Navier-Stokes equations explicitly by using the Chapman-Enskog expansion directly. Recently a comparative study of the performance of the LBE and GKS for nearly incompressible flow over a square cylinder has been conducted [14].

Originally, both LBE and GKS were designed for continuum flows. Extensions to rarefied gas flows have been developed recently. For example, the LBE with high-order moments or effective relaxation times have been proposed for flows with finite Knudsen numbers [6–8,15], while gas kinetic schemes with high-order expansions (Burnet and super-Burnet) are used for nonequilibrium flow study [16,17]. However, these improvements are still limited to weak nonequilibrium flows. Recently, a unified GKS (UGKS) method for all Knudsen number flows has been successfully constructed [4]. In UGKS, the gas distribution function at discrete particle velocities is numerically updated, as well as the conserved flow variables inside each control volume. However, the use of discrete velocities to represent a Maxwellian distribution may introduce conservation error in the discrete collision operator when updating the distribution function, although the conservation is precisely satisfied in the update of conserved variables. With sufficient number of discrete velocities, the UGKS is able to present satisfactory solutions for both continuum and rarefied flows efficiently and accurately [4,18]. Recently, the UGKS framework has been adopted in the construction of an asymptotic preserving (AP) scheme for radiative transfer problems [19].

In this series of work, we aim to develop a type of discrete unified gas kinetic scheme (DUGKS) which combines the advantages of both LBE and UGKS methods, and to enlarge the applicable flow regime of the LBE method. First, the DUGKS is a finite-volume scheme with flexible mesh adaptation, just like the GKS. Second, the evaluation of the flux at a cell interface in DUGKS is simplified by employing a transformation of distribution function with collision effect, which is used similarly in the LBE. Finally, by expanding the Maxwellian distribution into a series of velocity polynomials and choosing suitable discrete velocities, the DUGKS keeps its conservation properties in the discrete collision operator. The current paper presents the basic ingredients in DUGKS for smooth isothermal continuum and rarefied flow computations. The scheme for the general thermal flow will be presented in subsequent papers.

II. DISCRETE UNIFIED GAS-KINETIC SCHEME

A. Updating rule

The starting point of the proposed DUGKS is the Boltzmann equation with the Bhatnagar-Gross-Krook (BGK)

*zlguo@mail.hust.edu.cn
†makxu@ust.hk
‡ruijie.wang@ust.hk

collision model [20],

$$\frac{\partial f}{\partial t} + \boldsymbol{\xi}\cdot\nabla f = \Omega \equiv -\frac{1}{\tau}[f - f^{\rm eq}], \tag{1}$$

where $f = f(\boldsymbol{x},\boldsymbol{\xi},t)$ is the velocity distribution function for particles moving with velocity $\boldsymbol{\xi}$ at position $\boldsymbol{x}$ and time t, τ is the relaxation time, and $f^{\rm eq}$ is the Maxwellian equilibrium distribution function,

$$f^{\rm eq} = \frac{\rho}{(2\pi RT)^{D/2}}\exp\left(-\frac{|\boldsymbol{\xi}-\boldsymbol{u}|^2}{2RT}\right), \tag{2}$$

where R is the gas constant, D is the spatial dimension, ρ is the density, $\boldsymbol{u}$ is the fluid velocity, and T is the temperature. The conservative flow variables are the moments of the distribution function,

$$\boldsymbol{W} = \begin{pmatrix}\rho\\ \rho\boldsymbol{u}\\ \rho E\end{pmatrix} = \int \boldsymbol{\psi}(\boldsymbol{\xi}) f\, d\boldsymbol{\xi}, \tag{3}$$

where $\rho E = \rho(u^2 + DRT)/2$ is the total energy, and $\boldsymbol{\psi} = (1,\boldsymbol{\xi},\xi^2/2)^T$ is the collision invariant. Note that the BGK model gives a fixed Prandtl number (Pr = 1). Other types of equilibrium distribution functions, such as the Shakhov model [21] or the ellipsoidal statistical model [22], can be employed as well to adjust the Prandtl number.

Like the original GKS, the present scheme is also a finite-volume method. First, the flow domain is divided into a set of control volumes. As an illustration, a one-dimensional schematic diagram is shown in Fig. 1. Integrating Eq. (1) on a control volume V_j centered at $\boldsymbol{x}_j$ from time t_n to $t_{n+1} = t_n + \Delta t$ (the time step Δt is assumed to be a constant in the present work), one can obtain

$$f_j^{n+1} - f_j^n + \frac{\Delta t}{|V_j|}F^{n+1/2} = \frac{\Delta t}{2}\left[\Omega_j^{n+1} + \Omega_j^n\right], \tag{4}$$

where the midpoint rule for the integration of the convection term and trapezoidal rule for the collision term are used, respectively, and

$$F^{n+1/2} = \int_{\partial V_j} (\boldsymbol{\xi}\cdot\boldsymbol{n}) f(\boldsymbol{x},t_{n+1/2})\, d\boldsymbol{S} \tag{5}$$

is the microflux across the cell interface, where $|V_j|$ and ∂V_j are the volume and surface of cell V_j, $\boldsymbol{n}$ is the outward unit vector normal to the surface, and f_j and Ω_i are the

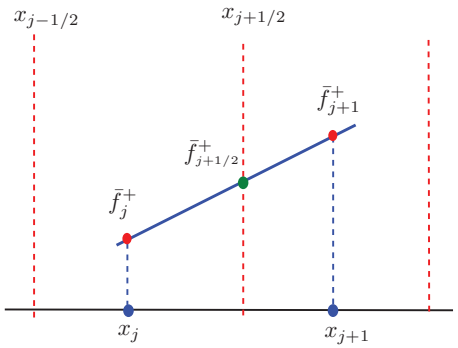

FIG. 1. (Color online) Schematic of one-dimensional cell geometry.

cell-averaged values of the distribution function and collision term, respectively, e.g.,

$$f_j^n = \frac{1}{|V_j|}\int_{V_j} f(\boldsymbol{x},\boldsymbol{\xi},t_n)\, d\boldsymbol{x}. \tag{6}$$

Note that the update of f_j, as shown in Eq. (4), is implicit in that the unknown macroscopic conserved variables $\boldsymbol{W}$ at t_{n+1} are required to evaluate $f^{\rm eq}$ in the collision term Ω_j^{n+1}. In order to remove this implicit treatment of the source term, a new distribution function is introduced,

$$\tilde{f} = f - \frac{\Delta t}{2}\Omega = \frac{2\tau+\Delta t}{2\tau}f - \frac{\Delta t}{2\tau}f^{\rm eq}. \tag{7}$$

Then Eq. (4) can be rewritten as

$$\tilde{f}_j^{n+1} = \tilde{f}_j^{+,n} - \frac{\Delta t}{|V_j|}F^{n+1/2}, \tag{8}$$

where

$$\tilde{f}^+ = \frac{2\tau-\Delta t}{2\tau+\Delta t}\tilde{f} + \frac{2\Delta t}{2\tau+\Delta t}f^{\rm eq}. \tag{9}$$

Since the collision operator conserves mass, momentum, and energy, the conserved variables can be computed from $\tilde{f}$,

$$\boldsymbol{W} = \int \boldsymbol{\psi}\tilde{f} d\boldsymbol{\xi}. \tag{10}$$

With these facts, in the DUGKS we will track the evolution of the distribution function $\tilde{f}$ instead of the original one.

The key point in updating $\tilde{f}$ according to Eq. (8) is to evaluate the flux $F^{n+1/2}$. In order to get that, we first integrate the Boltzmann equation within a half time step $h = \Delta t/2$ along the characteristic line with the end point ($\boldsymbol{x}_b$) located at the cell interface ($x_b = x_{j+1/2}$ in the one-dimensional case, see Fig. 1),

$$\begin{aligned} &f(\boldsymbol{x}_b,\boldsymbol{\xi},t_n+h) - f(\boldsymbol{x}_b-\boldsymbol{\xi}h,\boldsymbol{\xi},t_n)\\ &\quad = \frac{h}{2}\left[\Omega(\boldsymbol{x}_b,\boldsymbol{\xi},t_n+h) + \Omega(\boldsymbol{x}_b-\boldsymbol{\xi}h,\boldsymbol{\xi},t_n)\right], \end{aligned} \tag{11}$$

where the trapezoidal rule is again used to evaluate the collision term. Then, similar to the treatment in Eq. (4), we introduce another distribution function $\bar{f}$ to remove the implicity in Eq. (11),

$$\bar{f} = f - \frac{h}{2}\Omega = \frac{2\tau+h}{2\tau}f - \frac{h}{2\tau}f^{\rm eq}, \tag{12}$$

or

$$f = \frac{2\tau}{2\tau+h}\bar{f} + \frac{h}{2\tau+h}f^{\rm eq}. \tag{13}$$

As a result, Eq. (11) gives

$$\bar{f}(\boldsymbol{x}_b,\boldsymbol{\xi},t_n+h) = \bar{f}^+(\boldsymbol{x}_b-\boldsymbol{\xi}h,\boldsymbol{\xi},t_n), \tag{14}$$

where

$$\bar{f}^+ = \frac{2\tau-h}{2\tau+h}\bar{f} + \frac{2h}{2\tau+h}f^{\rm eq}. \tag{15}$$

Now the focus is on determining $\bar{f}^+(\boldsymbol{x}_b-\boldsymbol{\xi}h,\boldsymbol{\xi},t_n)$. With the Taylor expansion around the cell interface $\boldsymbol{x}_b$, for smooth flows, $\bar{f}^+(\boldsymbol{x}_b-\boldsymbol{\xi}h,\boldsymbol{\xi},t_n)$ can be approximated as

$$\bar{f}^+(\boldsymbol{x}_b-\boldsymbol{\xi}h,\boldsymbol{\xi},t_n) = \bar{f}^+(\boldsymbol{x}_b,\boldsymbol{\xi},t_n) - \boldsymbol{\xi}h\cdot\boldsymbol{\sigma}_b, \tag{16}$$

where $\bar{f}^+(\boldsymbol{x}_b,\boldsymbol{\xi},t_n)$ and the gradient $\boldsymbol{\sigma}_b = \nabla \bar{f}^+(\boldsymbol{x}_b,\boldsymbol{\xi},t_n)$ at the cell interface can be approximated by linear interpolations. For example, in the one-dimensional case shown in Fig. 1, the reconstructions become

$$\sigma_{j+1/2} = \frac{\bar{f}^+(x_{j+1},\xi,t_n) - \bar{f}^+(x_j,\xi,t_n)}{x_{j+1}-x_j}, \tag{17a}$$

$$\bar{f}^+(x_{j+1/2},\xi,t_n) = \bar{f}^+(x_j,\xi,t_n) + \sigma_{j+1/2}(x_{j+1/2}-x_j). \tag{17b}$$

Based on Eqs. (14) and (16), we can get

$$\bar{f}(\boldsymbol{x}_b,\boldsymbol{\xi},t_n+h) = \bar{f}^+(\boldsymbol{x}_b,\boldsymbol{\xi},t_n) - \boldsymbol{\xi} h\cdot\boldsymbol{\sigma}_b, \tag{18}$$

from which the conserved variables at the cell interface can be obtained,

$$\boldsymbol{W}(\boldsymbol{x}_b,t_n+h) = \int \boldsymbol{\psi}\,\bar{f}(\boldsymbol{x}_b,\boldsymbol{\xi},t_n+h)\,d\boldsymbol{\xi}. \tag{19}$$

As a result, the equilibrium distribution function $f^{\rm eq}(\boldsymbol{x}_b,t_n+h)$ is fully determined, and the original distribution function can be obtained from $\bar{f}(\boldsymbol{x}_b,t_n+h)$ as well:

$$f(\boldsymbol{x}_b,t_n+h) = \frac{2\tau}{2\tau+h}\bar{f}(\boldsymbol{x}_b,t_n+h) + \frac{h}{2\tau+h}f^{\rm eq}(\boldsymbol{x}_b,t_n+h). \tag{20}$$

With the determination of the distribution function at a cell interface, the microflux F can be fully evaluated according to Eq. (5). The update of the distribution function $\tilde{f}$ can then be done according to Eq. (8).

It should be noted that the distribution functions $\tilde{f}$, $\bar{f}$, $\tilde{f}^+$, and $\bar{f}^+$ are all related to the original distribution function f and the Maxwellian $f^{\rm eq}$ (see Appendix A). Particularly, the following relations will be used in computation:

$$\bar{f}^+ = \frac{2\tau-h}{2\tau+\Delta t}\tilde{f} + \frac{3h}{2\tau+\Delta t}f^{\rm eq}, \tag{21}$$

$$\tilde{f}^+ = \frac{4}{3}\bar{f}^+ - \frac{1}{3}\tilde{f}. \tag{22}$$

In summary, the update of $\tilde{f}$ from t to $t+\Delta t$ in the discrete unified gas kinetic schemes (DUGKS) is the following:

$$\begin{aligned}\tilde{f}(\boldsymbol{x}_j,t) &\xrightarrow{(21),(22)} \bar{f}^+(\boldsymbol{x}_j,t) \quad\text{and}\quad \tilde{f}^+(\boldsymbol{x}_j,t)\\ &\longrightarrow \bar{f}^+(\boldsymbol{x}_b,t) \quad\text{and}\quad \boldsymbol{\sigma}_b \xrightarrow{(18)} \bar{f}(\boldsymbol{x}_b,t_n+h)\\ &\xrightarrow{(19)} \boldsymbol{W}(\boldsymbol{x}_b,t+h) \xrightarrow{(20)} f(\boldsymbol{x}_b,t+h)\\ &\xrightarrow{(5)} F(\boldsymbol{x}_b,t+h) \xrightarrow{(8)} \tilde{f}(\boldsymbol{x}_j,t+\Delta t).\end{aligned}$$

The above scheme is valid in a continuous particle velocity space $\boldsymbol{\xi}$. In practical computations, $\boldsymbol{\xi}$ will be replaced by discrete particle velocities, which will be presented in the next section.

B. Discretization of the particle velocity space

The discretization of the particle velocity space is important for any discrete ordinate method. In DUGKS, the velocity space is divided into a finite set of subcells, i.e.,

$$\boldsymbol{\xi} \in \bigcup_{\boldsymbol{i}=-\boldsymbol{N}}^{\boldsymbol{N}} [\boldsymbol{\xi}_{\boldsymbol{i}-1},\boldsymbol{\xi}_{\boldsymbol{i}}],$$

where $\boldsymbol{i} = (i_1,i_2,\ldots,i_D)$, and $\boldsymbol{N} = (N_1,N_2,\ldots,N_D)$, with N_i being positive integers.

With the discrete velocity space, the moments of a continuous distribution function have to be expressed as discrete moments,

$$\boldsymbol{m} = \int \phi(\boldsymbol{\xi})f(\boldsymbol{\xi})d\boldsymbol{\xi} = \sum_{\boldsymbol{i}=-\boldsymbol{N}}^{\boldsymbol{N}} w_{\boldsymbol{i}}\phi(\boldsymbol{\xi}_{\boldsymbol{i}})f(\boldsymbol{\xi}_{\boldsymbol{i}}), \tag{23}$$

where ϕ is a polynomial of the particle velocity $\boldsymbol{\xi}$ and $w_{\boldsymbol{i}}$ is the weight of the numerical quadrature at the discrete velocity $\boldsymbol{\xi}_{\boldsymbol{i}}$. In general, the quadrature cannot present the same results as the exact moments of a continuous distribution function due to numerical errors, and the difference can be reduced by increasing the number of discrete points. Particularly with discrete velocities, the BGK collision operator may not be fully conservative [23–25], i.e.,

$$\boldsymbol{W} \equiv \sum_{\boldsymbol{i}=-\boldsymbol{N}}^{\boldsymbol{N}} w_{\boldsymbol{i}}\boldsymbol{\psi}(\boldsymbol{\xi}_{\boldsymbol{i}})f(\boldsymbol{\xi}_{\boldsymbol{i}}) \neq \sum_{\boldsymbol{i}=-\boldsymbol{N}}^{\boldsymbol{N}} w_{\boldsymbol{i}}\boldsymbol{\psi}(\boldsymbol{\xi}_{\boldsymbol{i}})f^{\rm eq}(\boldsymbol{\xi}_{\boldsymbol{i}},\boldsymbol{W}). \tag{24}$$

However, one can define a discrete Maxwellian distribution with some free parameters to be determined with the conservation requirement [24], where a nonlinear system needs to be solved.

In the following, a simple method to ensure the conservation for low-speed isothermal flow is proposed, which is inspired by the LBE method. At a constant temperature T and low fluid velocity, i.e., the Mach number $Ma \approx |\boldsymbol{u}|/\sqrt{RT} \ll 1.0$, the Maxwellian distribution can be approximated by its Taylor or Hermite expansion up to second order of Ma, the same as the LBE method [15,23,26]:

$$f^{\rm eq}(\boldsymbol{\xi}) = \frac{\rho}{(2\pi RT)^{D/2}}\exp\left(-\frac{|\boldsymbol{\xi}|^2}{2RT}\right) \times\left[1+\frac{\boldsymbol{\xi}\cdot\boldsymbol{u}}{RT}+\frac{(\boldsymbol{\xi}\cdot\boldsymbol{u})^2}{2(RT)^2}-\frac{|\boldsymbol{u}|^2}{2RT}\right]. \tag{25}$$

Then the conservations of mass and momentum can be realized by choosing an appropriate quadrature rule with the following moment evaluation:

$$\int \psi(\boldsymbol{\xi})f^{\rm eq}d\boldsymbol{\xi} = \sum_{\boldsymbol{i}} w_{\boldsymbol{i}}\psi(\boldsymbol{\xi}_{\boldsymbol{i}})f^{\rm eq}(\boldsymbol{\xi}_{\boldsymbol{i}}), \quad \psi = 1,\boldsymbol{\xi}. \tag{26}$$

From the expression of Eq. (25), it is natural to choose the Gauss-Hermite quadrature with the weight function $(2\pi RT)^{-D/2}\exp(-|\boldsymbol{\xi}|^2/2RT)$. Assuming that the abscissas and the corresponding weights of the chosen quadrature are $\boldsymbol{\xi}_{\boldsymbol{i}}$ and $W_{\boldsymbol{i}}$, respectively, then we can identify the weights used in evaluating the discrete moments in Eq. (23):

$$w_{\boldsymbol{i}} = W_{\boldsymbol{i}}(2\pi RT)^{D/2}\exp\left(\frac{|\boldsymbol{\xi}_{\boldsymbol{i}}|^2}{2RT}\right). \tag{27}$$

Usually, it is difficult to obtain Gauss-Hermite formulas as $D>1$, but the tensor product of one-dimensional formulas can be used to define a high-dimensional formula. Assuming that ξ_i and W_i are the abscissas and weights of a one-dimensional quadrature, the abscissas and weights of a D-dimensional Gaussian-Hermite quadrature become

$$\boldsymbol{\xi}_{\boldsymbol{i}} = \left(\xi_{i_1},\xi_{i_2},\ldots,\xi_{i_D}\right), \qquad W_{\boldsymbol{i}} = W_{i_1}W_{i_2}\ldots W_{i_D}, \tag{28}$$

where $\boldsymbol{i} = i_1 i_2 \ldots i_D$.

It should be noted that the abscissas of Gauss-Hermite quadrature are not uniformly distributed. In highly nonequilibrium flow computations, the discrete velocities determined in this way may not be appropriate due to the significant deviation of f from the equilibrium. In such cases a uniformly distributed discrete velocity is preferred, such as using Gauss or Newton-Cotes rules.

C. Boundary conditions

Appropriate boundary conditions should be specified for the discrete distribution functions at solid walls. Two types of kinetic boundary conditions will be considered here: the bounce-back rule and the diffuse-scattering rule. The former is for a no-slip wall, which assumes a particle just reverses its velocity after hitting the wall. Specifically, assuming the wall is located at a cell interface $\boldsymbol{x}_w$, then the distribution functions $f(\boldsymbol{x}_w,\boldsymbol{\xi}_i,t+h)$ for particles moving towards the wall, i.e., $\boldsymbol{\xi}\cdot\boldsymbol{n}\leqslant 0$ with $\boldsymbol{n}$ being the unit vector normal to the wall pointing to the cell, can be constructed following the procedure described in Sec. II A, and those for particles leaving the wall are determined as

$$f(\boldsymbol{x}_w,\boldsymbol{\xi}_i,t+h)=f(\boldsymbol{x}_w,-\boldsymbol{\xi}_i,t+h)+2\rho_w\frac{W_i}{w_i}\frac{\boldsymbol{\xi}_i\cdot\boldsymbol{u}_w}{RT},\quad \boldsymbol{\xi}_i\cdot\boldsymbol{n}>0, \tag{29}$$

where $\boldsymbol{u}_w$ is the wall velocity, and ρ_w is the density at the wall determined by the definition of the density,

$$\rho_w=\left[1-\frac{2}{RT}\sum_{\boldsymbol{\xi}_i\cdot\boldsymbol{n}>0}W_i\boldsymbol{\xi}_i\cdot\boldsymbol{u}_w\right]^{-1}\times\left[\sum_{\boldsymbol{\xi}_i\cdot\boldsymbol{n}=0}w_i f(\boldsymbol{\xi}_i)+2\sum_{\boldsymbol{\xi}_i\cdot\boldsymbol{n}<0}w_i f(\boldsymbol{\xi}_i)\right]. \tag{30}$$

For nearly incompressible flow, ρ_w can be approximated well by the constant average density. The above method is also widely used in LBE for no-slip walls [27].

The diffuse-scattering rule assumes the velocity distribution is Maxwellian, with the wall temperature and velocity, once the particles reflect from the wall, as follows:

$$f(\boldsymbol{x}_w,\boldsymbol{\xi}_i,t+h)=f^{\mathrm{eq}}(\boldsymbol{\xi}_i;\rho_w,\boldsymbol{u}_w),\quad \boldsymbol{\xi}_i\cdot\boldsymbol{n}>0, \tag{31}$$

where the density ρ_w is determined by the condition that no particles can go through the wall, i.e.,

$$\sum_{\boldsymbol{\xi}_i\cdot\boldsymbol{n}>0}(\boldsymbol{\xi}\cdot\boldsymbol{n})f^{\mathrm{eq}}(\boldsymbol{\xi}_i;\rho_w,\boldsymbol{u}_w)+\sum_{\boldsymbol{\xi}_i\cdot\boldsymbol{n}<0}(\boldsymbol{\xi}\cdot\boldsymbol{n})f(\boldsymbol{x}_w,\boldsymbol{\xi}_i,t+h)=0, \tag{32}$$

which gives

$$\rho_w=-\left[\sum_{\boldsymbol{\xi}_i\cdot\boldsymbol{n}>0}(\boldsymbol{\xi}\cdot\boldsymbol{n})f^{\mathrm{eq}}(\boldsymbol{\xi}_i;1,\boldsymbol{u}_w)\right]^{-1}\times\sum_{\boldsymbol{\xi}_i\cdot\boldsymbol{n}<0}(\boldsymbol{\xi}\cdot\boldsymbol{n})f(\boldsymbol{x}_w,\boldsymbol{\xi}_i,t+h). \tag{33}$$

D. Algorithm

In the following, we list the computation procedure for the updating of the discrete distribution function. In the computation, the weight coefficients w_i can be absorbed into the discrete distribution functions, i.e.,

$$f_i=w_i f(\boldsymbol{\xi}_i),\quad f_i^{\mathrm{eq}}=w_i f^{\mathrm{eq}}(\boldsymbol{\xi}_i).$$

Particularly, if the Gauss-Hermite quadrature is employed, the expanded discrete equilibrium distribution function takes a simple formulation,

$$f_i^{\mathrm{eq}}=W_i\left[1+\frac{\boldsymbol{\xi}\cdot\boldsymbol{u}}{RT}+\frac{(\boldsymbol{\xi}\cdot\boldsymbol{u})^2}{2(RT)^2}-\frac{|\boldsymbol{u}|^2}{2RT}\right], \tag{34}$$

which is very similar to that in LBE. Note that in the proposed DUGKS, the distribution $\tilde{f}$ is recorded instead of the original one, so that the density and velocity can be evaluated as

$$\rho=\sum_{i=-N}^{N}\tilde{f}_i,\quad \rho\boldsymbol{u}=\sum_{i=-N}^{N}\boldsymbol{\xi}_i\tilde{f}_i. \tag{35}$$

The update of $\tilde{f}_i$ is the same as that for the continuous case presented in Sec. II A. Specifically, with initialized $\tilde{f}_{j,i}^0$ in all cells centered at $\boldsymbol{x}_j$ ($j=1,2,\ldots,J$, with J being the total number of cells), the procedure of the DUGKS at each time step t_n reads as follows:

(1) Compute the distribution functions $\bar{f}_{j,i}^{+,n}$ in each cell, Eq. (21).

(2) Compute the distribution functions $\bar{f}_i^{n+1/2}(\boldsymbol{x}_b)$, Eq. (18).

(3) Compute the density $\rho^{n+1/2}(\boldsymbol{x}_b)$ and velocity $\boldsymbol{u}^{n+1/2}(\boldsymbol{x}_b)$ at the interface from $\bar{f}_i^{n+1/2}(\boldsymbol{x}_b)$, Eq. (19).

(4) Compute the original distribution function $f_i^{n+1/2}(\boldsymbol{x}_b)$, Eq. (13).

(5) Compute the microflux across the cell interfaces from $f_i^{n+1/2}(\boldsymbol{x}_b)$, Eq. (5).

(6) Update the distribution functions $\tilde{f}_{j,i}^{n+1}$ via Eq. (8), where $\tilde{f}^+$ is computed according to Eq. (22).

III. PROPERTIES OF THE DUGKS

It is interesting to discuss the properties of the present DUGKS. First, the DUGKS is a multidimensional scheme in the reconstruction of the distribution function at the cell interface. As mentioned in Ref. [28], it is not straightforward to develop a multidimensional finite-volume scheme based on the macroscopic fluid equations [3]. In the DUGKS, instead of waves the particle is followed by its trajectory in a multidimensional basis.

Second, the DUGKS exhibits the asymptotic preserving (AP) property. As mentioned in Ref. [4], a kinetic scheme is AP if (a) the time step is not restricted by the particle collision time in the continuum regime; (b) it preserves the discrete analogy of the Chapman-Enskog expansion as the Knudsen number goes to 0; and (c) the scheme has at least second-order accuracy in both continuum and free-molecular regimes. For the present DUGKS, it couples the advection and collision processes of particle transport, and the time step Δt is independent of the collision time τ for all flow regimes, which is determined by

the Courant-Friedrichs-Lewy (CFL) condition [4],

$$\Delta t = \alpha \frac{\Delta x}{C}, \tag{36}$$

where α is the CFL number, Δx is the minimal grid spacing, and C is in the order of the maximal discrete velocity. For continuum flow, C can be taken as the sound speed of the flow. Therefore, the DUGKS satisfies the condition (a). For condition (b), as shown in Appendix B, in the continuum limit as $\tau \ll \Delta t$ the reconstructed distribution function at the cell interface given by Eq. (20) goes to

$$f(\boldsymbol{x}_b,\boldsymbol{\xi},t_n+h) \approx f^{\rm eq}(\boldsymbol{x}_b,\boldsymbol{\xi},t) - \tau(\partial_t + \boldsymbol{\xi}\cdot\nabla) f^{\rm eq}(\boldsymbol{x}_b,\boldsymbol{\xi},t) + h\partial_t f^{\rm eq}(\boldsymbol{x}_b,\boldsymbol{\xi},t), \tag{37}$$

which recovers the Chapman-Enskog approximation for the Navier-Stokes solution [3,4]. On the other hand, in a highly nonequilibrium limit when the relaxation time is much larger than the time step ($\tau \gg \Delta t$), Eq. (20), together with Eqs. (14), (15), and (12), gives that $f(\boldsymbol{x}_b,t_n+h) \approx f(x_b-\boldsymbol{\xi}h,t_n)$, which presents the collisionless limit. Regarding the accuracy, the use of the midpoint and trapezoidal rules in Eqs. (4) and (11), as well as the linear reconstruction of the distribution function at the cell interface, ensures a second-order accuracy in both space and time. The above arguments indicate that the present DUGKS is an asymptotic preserving scheme.

Now let us compare the present DUGKS with the original UGKS [4,18,28]. It is clear that the DUGKS shares many common features with the UGKS, such as the use of discrete velocity space and the AP property. However, the differences between these two schemes are also clear: First, in the original UGKS [4], both the conserved flow variables $\boldsymbol{W}$ and the discrete distribution functions are updated simultaneously in each control volume V_j, i.e.,

$$\boldsymbol{W}_j^{n+1} - \boldsymbol{W}_j^n + \frac{1}{|V_j|}\int_{t_n}^{t_{n+1}} \boldsymbol{\mathcal{F}}(t)\,dt = 0, \tag{38}$$

$$f_j^{n+1} = \left(1+\frac{\Delta t}{2\tau}\right)^{-1}\left[f_j^n + \frac{\Delta t}{2\tau} f_j^{\rm eq}(\boldsymbol{W}^{n+1}) + \frac{\Delta t}{2}\Omega_j^n - \frac{1}{|V_j|}\int_{t_n}^{t_{n+1}} F(t)\,dt\right], \tag{39}$$

where $\boldsymbol{\mathcal{F}} = \int_{\partial V_j} (\boldsymbol{\xi}\cdot\boldsymbol{n})\boldsymbol{\psi} f(\boldsymbol{x},\boldsymbol{\xi},t)\,d\boldsymbol{S}\,d\boldsymbol{\xi}$ and $F = \int_{\partial V_j}(\boldsymbol{\xi}\cdot\boldsymbol{n}) f(\boldsymbol{x},\boldsymbol{\xi},t)\,d\boldsymbol{S}$ are the macroscopic and microscopic fluxes across the cell interface, respectively. The distribution function $f(t)$ at the cell interface is reconstructed from an integral solution of the BGK model, which is similar to the BGK Navier-Stokes scheme [3]. On the other hand, in the present DUGKS the update of the conserved flow variables $\boldsymbol{W}$ are not required for the solution $\tilde{f}$. Also, in the calculation of the microscopic flux F, only the distribution function at the discrete half time step, i.e., $f(t+\Delta t/2)$, is needed and obtained explicitly through $\bar{f}$. With this technique the update of the distribution function in the DUGKS is much simplified.

The second main difference between the DUGKS and UGKS lies in the enforcement of the conservative property of the discrete collision operator. In the UGKS, the use of Maxwellian equilibrium with discrete velocities cannot ensure the conservation of the discrete collision operator rigorously [see Eq. (24)], even though the updated $\boldsymbol{W}$ in Eq. (38) satisfies the conservation precisely due to the use of $\sum_i w_i\boldsymbol{\psi}(\boldsymbol{\xi}_i)\Omega(\boldsymbol{\xi}_i) = 0$ inside each control volume. Consequently, the nonconservation property of the discrete collision operator may remain in the update of the distribution function in Eq. (39). On the contrary, with an expansion of the Maxwellian and suitable quadratures, the DUGKS can realize the conservation in the update of f (and so $\boldsymbol{W}$).

It is also interesting to compare the present DUGKS with the LBE method. The apparent common feature of both methods is the use of an expanded equilibrium distribution function, but the obvious difference between them is that LBE is a finite-difference scheme which uses a regular lattice coupled with the discrete velocities, while the DUGKS is a finite-volume scheme which can employ irregular meshes. Another difference is that the DUGKS can be easily applied to rarefied gas flows, while the original LBE is mainly designed for the Navier-Stokes equations. With the use of higher-order Gauss-Hermite quadratures, having discrete velocity sets which are usually incompatible with a regular lattice, the LBE can be extended to nonequilibrium flows [15]. We note that some finite-volume LBE discretizations (FV-LBE) (e.g., [29–32]) were also designed for solving the following discrete-velocity model:

$$\frac{\partial f_i}{\partial t} + \boldsymbol{\xi}_i\cdot\nabla f_i = \Omega(\boldsymbol{\xi}_i). \tag{40}$$

In FV-LBE, the transport term is usually discretized using the first-order upwinding approach. The analysis in Refs. [31,33] indicates that the FV-LBE method may suffer from severe numerical dissipation and the time step Δt is limited by the collision time τ, meaning that the AP property is not maintained in the FV-LBE method.

IV. NUMERICAL RESULTS

In this section, the DUGKS will be validated through some numerical tests. The tests include two parts. In the first part, two continuum flows are simulated and the results are compared with the analytical solutions or benchmark data. In the second part, the DUGKS will be used to study rarefied flows in the transition and free molecular regimes.

For continuum flows, the three-point Gauss-Hermite quadrature is used to evaluate the moments, which yields the following discrete velocities and associated weights ($D = 1$),

$$\xi_{-1} = -\sqrt{3RT}, \quad \xi_0 = 0, \quad \xi_1 = \sqrt{3RT}, \quad W_0 = 2/3, \quad W_{\pm1} = 1/6. \tag{41}$$

For higher-dimensional flows, the discrete velocities and weights are generated using the tensor product method described in Sec. II B. Furthermore, for continuum flows no-slip boundary conditions, which are realized by the bounce-back rule, are used at solid walls.

For the nonequilibrium microflows, the Knudsen number is defined as $\mathrm{Kn} = \lambda/L$, where λ and L are the mean free path and characteristic length of the flow, respectively. Here λ is related to the relaxation time τ through the viscosity coefficient, i.e.,

$$\lambda = \frac{\mu}{p}\sqrt{\frac{\pi RT}{2}} = \tau\sqrt{\frac{\pi RT}{2}}. \tag{42}$$

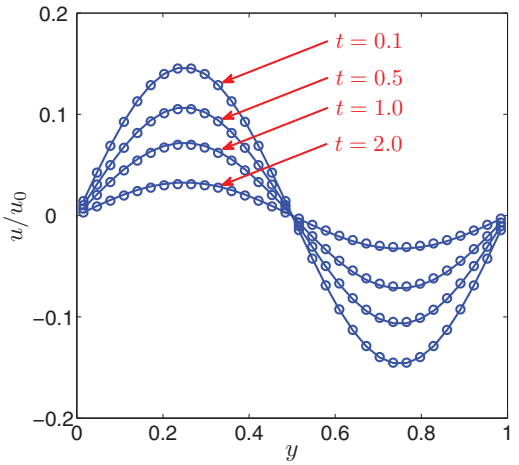

FIG. 2. (Color online) Velocity profiles at different times of the Taylor vortex flow.

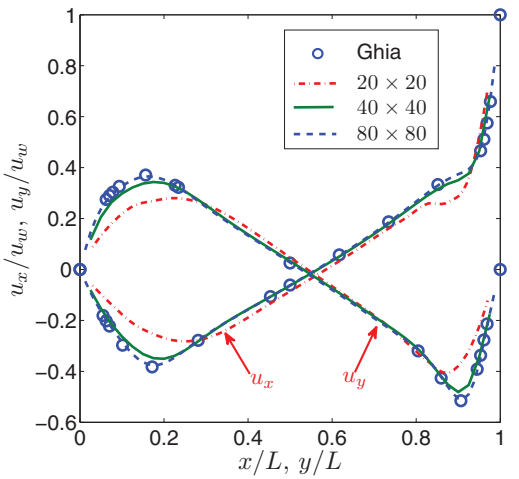

FIG. 3. (Color online) Velocity across the cavity center at Re = 1000 on uniform meshes.

Because of low fluid speed in microflows, the expanded equilibrium distribution function given by Eq. (25) is employed. The discrete velocities are chosen based on two types of quadratures, depending on the flow properties, i.e., the half range Gauss-Hermite quadrature [34,35] or the Newton-Cotes quadrature. The former is found to be able to give satisfactory predictions for flows close to the equilibrium, while the Newton-Cotes quadrature can give good predictions for nonequilibrium cases. Furthermore, the diffuse-scattering boundary condition is employed in the simulations of microflows.

A. Taylor vortex flow

The first test problem is the two-dimensional incompressible Taylor vortex flow in a periodic domain, which has the following analytical solution:

$$u(x,y,t) = -\frac{u_0}{A}\cos(Ax)\sin(By)e^{-\nu\alpha t}, \tag{43a}$$

$$v(x,y,t) = \frac{u_0}{B}\sin(Ax)\cos(By)e^{-\nu\alpha t}, \tag{43b}$$

$$p(x,y,t) = -\frac{u_0^2}{4}\left[\frac{\cos(2Ax)}{A^2} + \frac{\cos(2By)}{B^2}\right]e^{-2\nu\alpha t}, \tag{43c}$$

where u_0 is a constant, $\alpha = A^2 + B^2$, ν is the shear viscosity, and $\boldsymbol{u} = (u,v)$ and p are the velocity and pressure, respectively.

In our simulations, we set $A = B = 2\pi$, $\nu = 0.001$, $u_0 = 1.0$, and $RT = 100$, the computation domain is set to be $0 \leqslant x \leqslant 1$ and $0 \leqslant y \leqslant 1$, and the CFL number is set to be 0.5 unless stated otherwise. For this unsteady flow, the distribution function should be properly initialized by adopting the Navier-Stokes Chapman-Enskog expansion,

$$f(\boldsymbol{x},\boldsymbol{\xi},0) = f^{\mathrm{eq}} - \tau[\partial_t f^{\mathrm{eq}} + \boldsymbol{\xi}\cdot\nabla f^{\mathrm{eq}}], \tag{44}$$

where the temporal and spatial derivatives are evaluated using the analytical solution (43).

The velocity profiles at different times predicted by the DUGKS on a 32×32 uniform mesh are compared with the analytical solution in Fig. 2. It can be seen that the numerical results are in excellent agreement with the theoretical ones. To test the convergence order of the DUGKS, a set of simulations on different meshes have been done. In the simulations, the time step Δt is directly set to a small value (10^{-5}) in order to reduce the time error in the evaluation of spatial accuracy. The L_2 errors in velocity and pressure field are measured in Table I, where the L_2 error is defined by

$$E(\phi) = \frac{\sqrt{\sum_{x,y}|\phi(x,y,t) - \phi_e(x,y,t)|^2}}{\sqrt{\sum_{x,y}|\phi_e(x,y,t)|^2}}, \quad \phi = \boldsymbol{u} \ \text{ or } p, \tag{45}$$

where ϕ_e is the analytical value given by Eq. (43). Second-order convergency of the DUGKS is clearly confirmed.

B. Continuum cavity flow

The two-dimensional lid-driven cavity flow is a standard benchmark problem for validating numerical schemes. The geometry considered is a two-dimensional square cavity in the Cartesian coordinate system (x,y), with a top wall moving along the x direction with a constant velocity u_w and three

TABLE I. Error and convergence order in velocity and pressure ($\Delta t = 10^{-5}$).

N	16	32	64	128
$E(\boldsymbol{u})$	3.7533×10^{-2}	9.3909×10^{-3}	2.3438×10^{-3}	5.8156×10^{-4}
order	–	1.999	2.002	2.011
$E(p)$	7.6964×10^{-2}	2.0807×10^{-2}	4.3993×10^{-3}	1.2751×10^{-3}
order	–	1.887	2.242	1.787

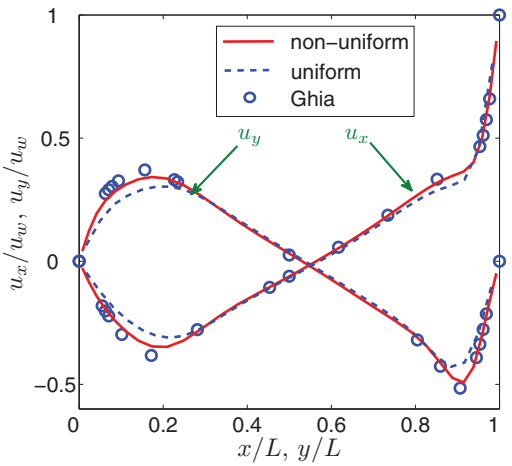

FIG. 4. (Color online) Velocity across the cavity center at Re = 1000 on nonuniform and uniform meshes (30 × 30).

fixed walls. The flow is characterized by the Reynolds number $\mathrm{Re} = Lu_w/\nu$, where L is the cavity length and ν is the shear viscosity of the fluid. In the simulations the driven velocity is set to be 0.1 and $RT = 1/3$ so that the Mach number is small in order to ensure nearly incompressible flow; the length of the cavity is taken to be 1.0, and the CFL number is set to be 0.5 in all cases unless stated otherwise. The top two corners are singular points, and in our simulations both are assumed to be stationary.

First, the DUGKS is used to simulate the flow at Re = 1000 on different uniform meshes. In Fig. 3 the velocity profiles, $\boldsymbol{u} = (u_x, u_y)$, across the cavity center are shown after the steady state is reached when the relative difference of the velocity at the cavity center between two successive 1000 steps is less than 10^{-6}. The benchmark data [37] are also included for comparison. It can be seen that the DUGKS solutions deviate from the benchmark data in the 30 × 30 coarse mesh case, which can be attributed to the large numerical dissipation with the unresolved boundary layer. The solution approaches the reference data as the grid resolution is increased, and good agreement between the DUGKS and the reference solutions can be observed on the 80 × 80 mesh.

The DUGKS also allows the use of nonuniform meshes, which can improve the prediction by using a locally refined mesh close to the boundary. To demonstrate this point, we repeat the above simulations with $N \times N = 30 \times 30$ mesh points in which the nodes (x_i, y_j) are generated by $x_i/L = (\zeta_i + \zeta_{i+1})/2$, $y_j/L = (\zeta_j + \zeta_{j+1})/2$ for $0 \leqslant i, j \leqslant N-1$, where ζ_i is defined by

$$\zeta_i = \frac{1}{2} + \frac{\tanh[a(i/N - 0.5)]}{2\tanh(a/2)}, \quad i = 0, 1, \ldots, N, \tag{46}$$

in which a is a constant that determines the distribution of the grid. Generally, a large value of a leads to a dense distribution of the mesh near the walls. In the current study a is set to be 2.5. The velocity profiles with this nonuniform mesh at Re = 1000 are shown in Fig. 4, as well as those with a uniform mesh of 30 × 30. The improvement in accuracy with the nonuniform mesh can be clearly observed, particularly in the transition regions near the walls.

The same cavity flow at Re = 1000 has been calculated as well using the D2Q9 LBE model with the same discrete velocity sets as DUGKS. The halfway bounce-back rule is employed to deal with the no-slip boundary conditions for both schemes on the four walls [27]. It is found that the computation blows up for LBE at Re = 1000 with a 64 × 64 uniform mesh. We also measure the maximum reachable Reynolds numbers of the DUGKS and LBE on a 80 × 80 uniform mesh. It is found that oscillations appear at Re = 1190 for LBE and the computation blows up at Re = 1195, while the DUGKS presents a convergent stable solution at Re = 4000 with a CFL number of 0.95. These results suggest that the DUGKS has a better numerical stability than the LBE using the same discrete velocity set and the same boundary treatments in the continuum flow limit. Furthermore, it is found that the velocity and pressure fields predicted by the LBE on an 80 × 80 uniform mesh at Re = 1000 have unphysical oscillations, while those of the DUGKS are smooth. As an example, the pressure contours predicted by both methods are shown in Fig. 5, where strong unphysical oscillations can be observed at the corners in the LBE solution, while the DUGKS solution is still reasonable.

C. Micro-Couette flow

Now we apply the DUGKS to the rarefied flow simulations. The first case is the microplanar Couette flow between two

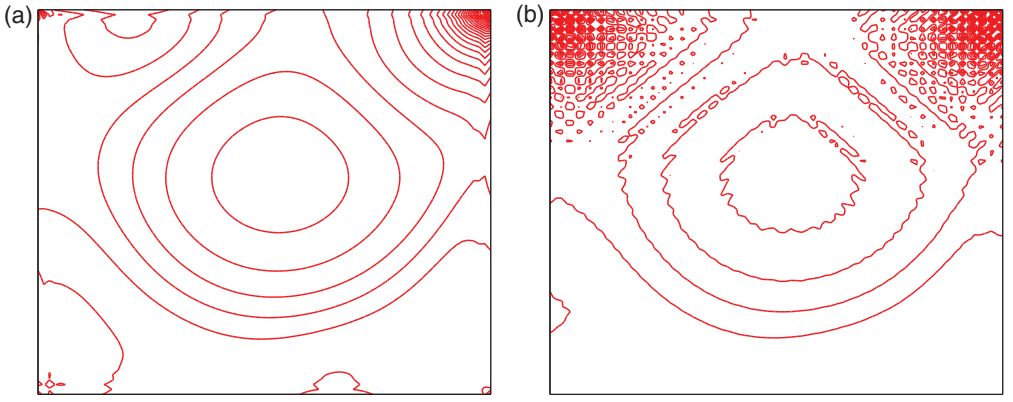

FIG. 5. (Color online) Pressure contours of the cavity flow at Re = 1000 on an 80 × 80 uniform mesh: (a) present DUGKS and (b) LBE.

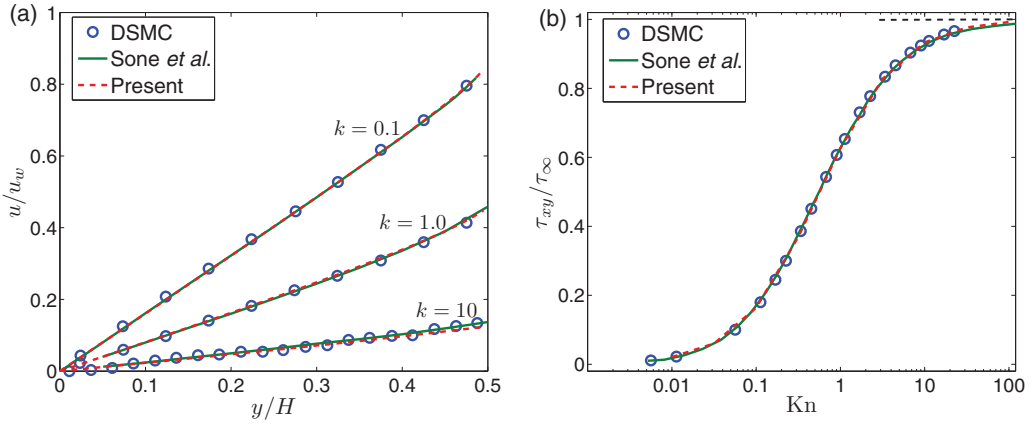

FIG. 6. (Color online) Velocity (a) and stress (b) of the Couette flow at different Knudsen numbers [$k = (\sqrt{\pi}/2)$Kn]. The DSMC data are from [38], and the solutions of the linearized Boltzmann equation are by Sone *et al.* [36].

parallel plates with a distance H. The top and bottom walls move with constant velocities u_w and $-u_w$, respectively, and periodic boundary conditions are imposed on the inlet and outlet of the channel. The micro-Couette flow has been studied using different methods, such as the linearized Boltzmann equation [36], the direct simulation Monte Carlo (DSMC) method [38], and the information preservation-DSMC (IP-DSMC) method [39], where benchmark solutions are available.

A number of simulations on the Couette flow from slip to free-molecular regimes are carried out. The 14-point half range Gauss-Hermite quadrature rule is used to determine the discrete velocities and weights [34]. Figure 6(a) shows

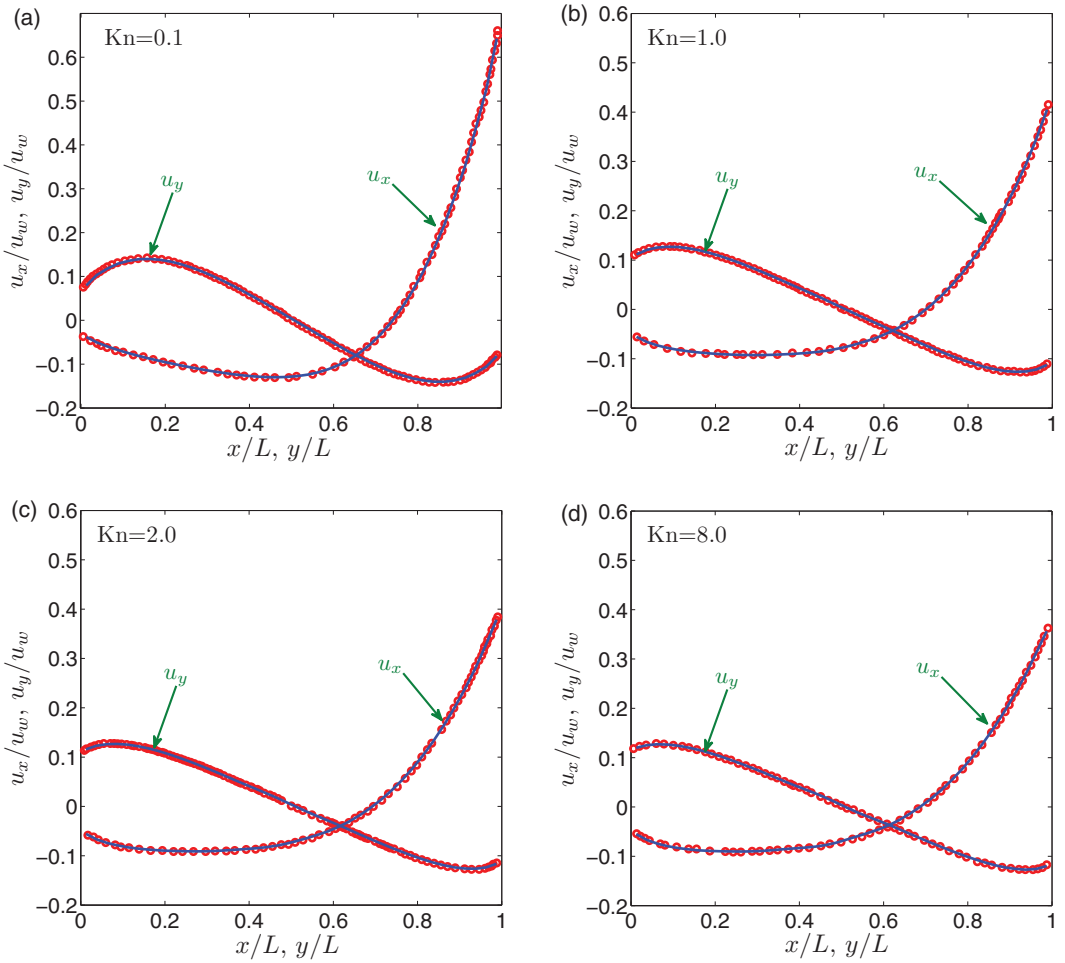

FIG. 7. (Color online) Velocity profiles across the cavity center at different Knudsen numbers. Open circle: DSMC data [40]; solid line: DUGKS results.

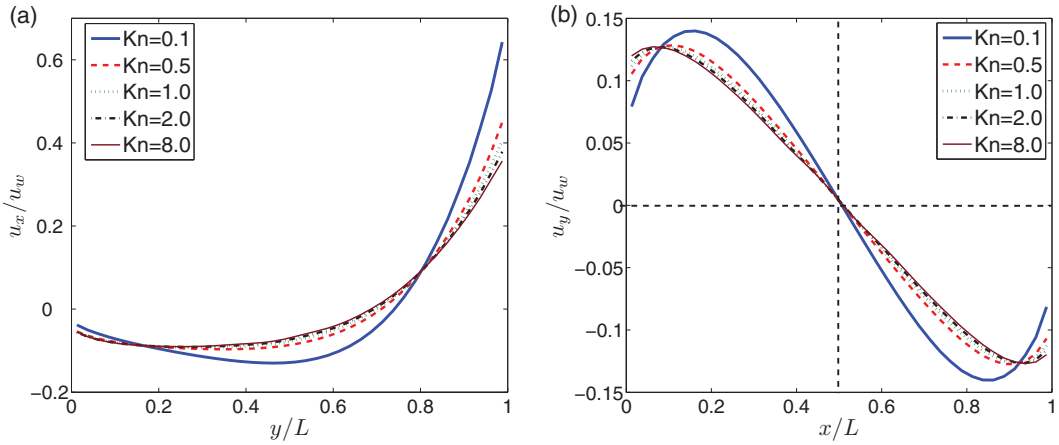

FIG. 8. (Color online) Velocity profiles across the cavity center at different Knudsen numbers.

the velocity profiles with $k = (\sqrt{\pi}/2)\mathrm{Kn} = 0.1$, 1, and 10, together with the DSMC data [38] and the solutions of the linearized Boltzmann equation [36]. Clearly, the DUGKS presents results which have good agreement with the reference solutions at all Knudsen numbers. Particularly, the nonlinearity of the velocity profiles near the wall is successfully captured. The shear stress τ_{xy}, normalized by the free-molecular stress $\tau_\infty = -\rho u_w \sqrt{2RT/\pi}$, is also measured and compared with the DSMC data [38] and the linearized Boltzmann solution [36]. As shown in Fig. 6(b), the results of the DUGKS are nearly indistinguishable from the benchmark solutions in the whole flow regimes.

D. Microcavity flow

The present DUGKS is also applied to the microcavity flow, which has been studied numerically based on the DSMC [40–42], linearized Boltzmann equation [43,44], and continuum hydrodynamic models [45,46]. The unified gas kinetic scheme has been applied here recently as well [28]. A typical feature of the microcavity flow is that the distribution function can become highly irregular with discontinuities induced by the walls, particularly around the four corners. The deviation from the local equilibrium increases with the Knudsen number, and unphysical oscillations may appear in the solution [43]. In order to reduce the oscillations, sufficient discrete velocity points must be employed to recover the irregularity of the distribution function. The difficulty in using the Gaussian quadrature method is that the distribution function is widely spanned in the whole velocity space and the weights for those far away from the average velocity can be rather small. Therefore, the contribution of these points in the Gaussian quadrature is diminishing. So, the use of Newton-Cotes quadrature is more appropriate in the highly nonequilibrium case.

In the simulations, the Knudsen number ranges from 0.1 to 8.0, and the velocity of the top wall u_w is given such that $u_w/\sqrt{\gamma RT} = 0.16$. The velocity space is discretized via the Newton-Cotes quadrature, with 100×100 nodes distributed uniformly in $[-4\sqrt{2RT}, 4\sqrt{2RT}] \times [-4\sqrt{2RT}, 4\sqrt{2RT}]$, which is sufficient for all cases in the current study. The physical space is discretized with 40×40 uniform mesh points, where the results are nearly identical to those on 80×80 mesh points. The CFL number is set to be 0.25 for all cases.

Figure 7 shows the velocity profiles across the cavity center for different Knudsen numbers, where the DSMC data with the same Mach number [40] are also included for comparison. It is observed that the DUGKS results agree excellently with the DSMC solutions in all cases. In order to identify the effects of the Knudsen number on the solutions, the velocity profiles are put together in Fig. 8. It is apparent that the velocity jump in both u_x and u_y along the wall increases with Kn. Interestingly, the slip velocity of u_x and u_y approaches a finite value at each wall. Also, the velocity component u_y across the horizontal centerline is almost symmetric in all Knudsen number cases, which means that the vortex center is close to the vertical line across the center of the cavity. Actually, the measured locations of the vortex center $(x_c/L, y_c/L)$ are about (0.506,0.741), (0.501,0.710), (0.500,0.700), (0.499,0.693), and (0.499,0.686) for Kn = 0.1, 0.5, 1, 2, and 8, respectively, where the vortex center moves downward and slightly leftward as Kn increases. These observations are consistent with the solutions from the DSMC and linearized Boltzmann equation [40,43]. These tests clearly show that the DUGKS is an accurate flow solver for rarefied flow simulations.

V. SUMMARY

In this paper, a finite-volume DUGKS is constructed for isothermal flow computations. The scheme shares many common features with the UGKS method in the continuum and rarefied flow study, such as possessing the asymptotic preserving properties. As a result, in the continuum flow regime the DUGKS can capture accurate Navier-Stokes solutions without imposing the constraint of the time step being less than the particle collision time. At the same time, accurate solutions can be obtained in the transition and free molecular regimes. In comparison with UGKS, due to the adoption of a new distribution function with the inclusion of a collision effect, the flux at a cell interface can be much more easily evaluated.

The DUGKS has been validated through several test cases, including both continuum and rarefied gas flows. Excellent

agreement has been obtained between the DUGKS solutions and the benchmark results in all cases. It is also found that based on the same number of discrete velocity points and boundary condition treatment, the DUGKS becomes more robust and accurate than the LBE method for the continuum flow computations, especially for the high-Reynolds-number cases.

The present DUGKS is targeted toward isothermal smooth flows, especially for comparison with the LBE method. Further development of DUGKS for compressible flow with heat transfer will be presented in subsequent papers.

ACKNOWLEDGMENTS

Z.L.G. acknowledges support from the National Natural Science Foundation of China (No. 51125024), and part of the work was carried out during his visit to the Hong Kong University of Science and Technology. K.X. was supported by the Hong Kong Research Grant Council (No. 621011) and the HKUST Research Fund (No. SRFI11SC05).

APPENDIX A: CONNECTIONS BETWEEN THE DISTRIBUTION FUNCTIONS

The defined distribution functions, i.e., $\tilde{f}$, $\bar{f}$, $\tilde{f}^+$, and $\bar{f}^+$, are all linear combinations of the original distribution function f and the equilibrium state $f^{\rm eq}$. This is clearly shown in the definitions of $\tilde{f}$ and $\bar{f}$. Here $\tilde{f}^+$ and $\bar{f}^+$ can be expressed as

$$\tilde{f}^+ = \frac{2\tau - \Delta t}{2\tau} f + \frac{\Delta t}{2\tau} f^{\rm eq}, \tag{A1}$$

$$\bar{f}^+ = \frac{2\tau - h}{2\tau} f + \frac{h}{2\tau} f^{\rm eq}. \tag{A2}$$

On the other hand, f can be expressed as linear combinations of the newly defined distribution functions and the equilibrium functions:

$$f = \frac{2\tau}{2\tau + \Delta t} \tilde{f} + \frac{\Delta t}{2\tau + \Delta t} f^{\rm eq}, \tag{A3}$$

$$f = \frac{2\tau}{2\tau + h} \bar{f} + \frac{h}{2\tau + h} f^{\rm eq}. \tag{A4}$$

In terms of the function $\tilde{f}$, $\tilde{f}^+$ and $\bar{f}^+$ can be expressed as

$$\tilde{f}^+ = \frac{2\tau - \Delta t}{2\tau + \Delta t} \tilde{f} + \frac{2\Delta t}{2\tau + \Delta t} f^{\rm eq}, \tag{A5}$$

$$\bar{f}^+ = \frac{2\tau - h}{2\tau + \Delta t} \tilde{f} + \frac{3h}{2\tau + \Delta t} f^{\rm eq}. \tag{A6}$$

Eliminating the equilibrium parts and using $h = \Delta t/2$, the above two equations give

$$\tilde{f}^+ = \tfrac{4}{3} \bar{f}^+ - \tfrac{1}{3} \tilde{f}. \tag{A7}$$

APPENDIX B: THE TIME-DEPENDENT CELL INTERFACE DISTRIBUTION FUNCTION IN THE CONTINUUM LIMIT

In order to figure out the distribution function used for the flux evaluation in the continuum limit, i.e., $f(\boldsymbol{x}_b, \boldsymbol{\xi}, t + h)$ given by Eq. (20), it is noticed that in the continuum limit the initial distribution function f can be approximated by the Chapman-Enskog expansion,

$$f(\boldsymbol{x}_b, \boldsymbol{\xi}, t) \approx f^{\rm eq} - \tau D_t f^{\rm eq} + O\left(D_t^2\right), \tag{B1}$$

where $D_t \equiv \partial_t + \boldsymbol{\xi} \cdot \nabla$. Furthermore, the time derivative and spatial gradient of $f^{\rm eq}$ can be related through the Euler equations [3], i.e.,

$$\partial_t f^{\rm eq} = \frac{\partial f^{\rm eq}}{\partial \boldsymbol{W}} \cdot \partial_t \boldsymbol{W} = -\frac{\partial f^{\rm eq}}{\partial \boldsymbol{W}} \cdot \nabla \cdot \boldsymbol{\mathcal{F}}^{\rm eq}, \tag{B2}$$

where $\boldsymbol{\mathcal{F}}^{\rm eq}$ is defined as

$$\boldsymbol{\mathcal{F}}^{\rm eq} = \int \boldsymbol{\psi} \boldsymbol{\xi} f^{\rm eq} d\boldsymbol{\xi}. \tag{B3}$$

Therefore, $f^{\rm eq}(\boldsymbol{x}_b, \boldsymbol{\xi}, t_n + h)$ can be approximated as

$$\begin{aligned} & f^{\rm eq}(\boldsymbol{x}_b, \boldsymbol{\xi}, t_n + h) \\ & \quad = f^{\rm eq}[\boldsymbol{\xi}, \boldsymbol{W}(\boldsymbol{x}_b, t_n + h)] \\ & \quad \approx f^{\rm eq}[\boldsymbol{\xi}, \boldsymbol{W}(\boldsymbol{x}_b, t)] + \frac{\partial f^{\rm eq}}{\partial \boldsymbol{W}} \cdot [\boldsymbol{W}(\boldsymbol{x}_b, t_n + h) - \boldsymbol{W}(\boldsymbol{x}_b, t_n)]. \end{aligned} \tag{B4}$$

From Eqs. (18) and (19), we have

$$\boldsymbol{W}(\boldsymbol{x}_b, t_n + h) = \boldsymbol{W}(\boldsymbol{x}_b, t_n) - h \nabla \cdot \boldsymbol{\mathcal{F}}(\boldsymbol{x}_b, t_n). \tag{B5}$$

Therefore,

$$\begin{aligned} f^{\rm eq}(\boldsymbol{x}_b, \boldsymbol{\xi}, t_n + h) &\approx f^{\rm eq}[\boldsymbol{\xi}, \boldsymbol{W}(\boldsymbol{x}_b, t)] - h \frac{\partial f^{\rm eq}}{\partial \boldsymbol{W}} \cdot \nabla \cdot \boldsymbol{\mathcal{F}}(\boldsymbol{x}_b, t_n) \\ &\approx f^{\rm eq}(\boldsymbol{x}_b, \boldsymbol{\xi}, t_n) + h \partial_t f^{\rm eq}(\boldsymbol{x}_b, \boldsymbol{\xi}, t_n). \end{aligned} \tag{B6}$$

It is clear that this is just the first-order Taylor expansion of $f^{\rm eq}(\boldsymbol{x}_b, \boldsymbol{\xi}, t_n + h)$ with respect to time. In other words, the calculation of $f^{\rm eq}(\boldsymbol{x}_b, \boldsymbol{\xi}, t_n + h)$ with $\boldsymbol{W}$ given by Eq. (19) is equivalent to the direct Taylor expansion, which has been used in the GKS as well for continuum flows [14]. However, it should be noted that the above derivation is valid for the continuum flow only.

With the above formulation, Eqs. (18), and (A2), Eq. (20) goes to

$$\begin{aligned} & f(\boldsymbol{x}_b, \boldsymbol{\xi}, t_n + h) \\ & = \frac{2\tau}{2\tau + h} \left\{ \frac{2\tau - h}{2\tau} [f(\boldsymbol{x}_b, \boldsymbol{\xi}, t_n) - h \boldsymbol{\xi} \cdot \nabla f(\boldsymbol{x}_b, \boldsymbol{\xi}, t_n)] + \frac{h}{2\tau} [f^{\rm eq}(\boldsymbol{x}_b, \boldsymbol{\xi}, t_n) - h \boldsymbol{\xi} \cdot \nabla f^{\rm eq}(\boldsymbol{x}_b, \boldsymbol{\xi}, t_n)] \right\} + \frac{h}{2\tau + h} f^{\rm eq}(\boldsymbol{x}_b, \boldsymbol{\xi}, t_n + h) \\ & = \frac{2\tau - h}{2\tau + h} f(\boldsymbol{x}_b, \boldsymbol{\xi}, t_n) + \frac{h}{2\tau + h} f^{\rm eq}(\boldsymbol{x}_b, \boldsymbol{\xi}, t_n) + \frac{h}{2\tau + h} f^{\rm eq}(\boldsymbol{x}_b, \boldsymbol{\xi}, t_n + h) - h \boldsymbol{\xi} \cdot \left[\frac{2\tau - h}{2\tau + h} \nabla f(\boldsymbol{x}_b, \boldsymbol{\xi}, t_n) + \frac{h}{2\tau + h} \nabla f^{\rm eq}(\boldsymbol{x}_b, \boldsymbol{\xi}, t_n) \right] \end{aligned}$$

$$
\begin{aligned}
&\approx \frac{2\tau - h}{2\tau + h}[f^{\mathrm{eq}}(\boldsymbol{x}_b,\boldsymbol{\xi},t_n) - \tau D_t f^{\mathrm{eq}}(\boldsymbol{x}_b,\boldsymbol{\xi},t_n)] + \frac{h}{2\tau + h} f^{\mathrm{eq}}(\boldsymbol{x}_b,\boldsymbol{\xi},t_n) + \frac{h}{2\tau + h}[f^{\mathrm{eq}}(\boldsymbol{x}_b,\boldsymbol{\xi},t_n) + h\partial_t f^{\mathrm{eq}}(\boldsymbol{x}_b,\boldsymbol{\xi},t_n)] \\
&\quad - h\boldsymbol{\xi}\cdot\left[\frac{2\tau - h}{2\tau + h}\nabla f^{\mathrm{eq}}(\boldsymbol{x}_b,\boldsymbol{\xi},t_n) + \frac{h}{2\tau + h}\nabla f^{\mathrm{eq}}(\boldsymbol{x}_b,\boldsymbol{\xi},t_n)\right] + O(\partial^2) \\
&= f^{\mathrm{eq}}(\boldsymbol{x}_b,\boldsymbol{\xi},t_n) - \tau D_t f^{\mathrm{eq}}(\boldsymbol{x}_b,\boldsymbol{\xi},t_n) + \frac{2\tau h}{2\tau + h} D_t f^{\mathrm{eq}}(\boldsymbol{x}_b,\boldsymbol{\xi},t_n) + \frac{h^2}{2\tau + h}\partial_t f^{\mathrm{eq}}(\boldsymbol{x}_b,\boldsymbol{\xi},t_n) - \frac{2\tau h}{2\tau + h}\boldsymbol{\xi}\cdot\nabla f^{\mathrm{eq}}(\boldsymbol{x}_b,\boldsymbol{\xi},t_n) + O(\partial^2) \\
&= f^{\mathrm{eq}}(\boldsymbol{x}_b,\boldsymbol{\xi},t_n) - \tau D_t f^{\mathrm{eq}}(\boldsymbol{x}_b,\boldsymbol{\xi},t_n) + h\partial_t f^{\mathrm{eq}}(\boldsymbol{x}_b,\boldsymbol{\xi},t_n) + O(\partial^2), \qquad \text{(B7)}
\end{aligned}
$$

which is precisely a time-dependent Chapman-Enskog Navier-Stokes distribution function.

[1] D. H. Rothman and S. Zaleski, *Lattice-Gas Cellular Automata: Simple Models of Complex Hydrodynamics* (Cambridge University Press, Cambridge, UK, 1997).
[2] S. Succi, *The Lattice Boltzmann Equation for Fluid Dynamics and Beyond* (Oxford University Press, Oxford, 2001).
[3] K. Xu, J. Comput. Phys. **171**, 289 (2001).
[4] K. Xu and J. C. Huang, J. Comput. Phys. **229**, 7747 (2010).
[5] P. J. Hoogerbrugge and J. M. V. A. Koelman, Europhys. Lett. **19**, 155 (1992).
[6] Z. L. Guo, T. S. Zhao, and Y. Shi, J. Appl. Phys. **99**, 074903 (2006).
[7] Y. H. Zhang, X. J. Gu, R. W. Barber, and D. R. Emerson, Phys. Rev. E **74**, 046704 (2006).
[8] Z. L. Guo, C. G. Zheng, and B. C. Shi, Phys. Rev. E **77**, 036707 (2008).
[9] Z. L. Guo, P. Asinari, and C. G. Zheng, Phys. Rev. E **79**, 026702 (2009).
[10] Z. L. Guo, B. C. Shi, and C. G. Zheng, Comput. Math. Appl. **61**, 3519 (2011).
[11] J. Meng, Y. H. Zhang, and X. W. Shan, Phys. Rev. E **83**, 046701 (2011).
[12] H. W. Liu, K. Xu, T. S. Zhu, and W. J. Ye, Comput. Fluids **67**, 115 (2012).
[13] S. Z. Chen, K. Xu, and C. B. Lee, Phys. Fluids **24**, 111701 (2012).
[14] Z. L. Guo, H. W. Liu, L.-S. Luo, and K. Xu, J. Comput. Phys. **227**, 4955 (2008).
[15] X. Shan, X. F. Yuan, and H. Chen, J. Fluid Mech. **550**, 413 (2006).
[16] T. Ohwada and K. Xu, J. Comput. Phys. **201**, 315 (2004); K. Xu and Z. H. Li, J. Fluid Mech. **513**, 87 (2004).
[17] K. Xu, Phys. Fluids **15**, 2077 (2003).
[18] S. Z. Chen, K. Xu, C. B. Li, and Q. D. Cai, J. Comput. Phys. **231**, 6643 (2012); R. J. Wang and K. Xu, Acta Mech. Sinica **28**, 1022 (2012).
[19] L. Mieussens, J. Comput. Phys. **253**, 138 (2013).
[20] P. L. Bhatnagar, E. P. Gross, and M. Krook, Phys. Rev. **94**, 511 (1954).
[21] E. M. Shakhov, Fluid Dyn. **3**, 95 (1968).
[22] L. H. Holway, Phys. Fluids **9**, 1658 (1966).
[23] L.-S. Luo, Comput. Phys. Commun. **129**, 63 (2000).
[24] L. Mieussens, J. Comput. Phys. **162**, 429 (2000).
[25] S. Pieraccini and G. Puppo, J. Sci. Comput. **32**, 1 (2007).
[26] X. He and L.-S. Luo, Phys. Rev. E **55**, R6333 (1997).
[27] A. J. C. Ladd, J. Fluid Mech. **271**, 285 (1994); **271**, 311 (1994).
[28] J.-C. Huang, K. Xu, and P. B. Yu, Commun. Comput. Phys. **12**, 662 (2012).
[29] F. Nannelli and S. Succi, J. Stat. Phys. **68**, 401 (1992).
[30] G. Peng, H. Xi, C. Duncan, and S. H. Chou, Phys. Rev. E **59**, 4675 (1999).
[31] S. Ubertini and S. Succi, Prog. Comput. Fluid Dyn. **5**, 85 (2005).
[32] M. Stiebler, J. Tölke, and M. Krafczyk, Comput. Fluids **35**, 814 (2006).
[33] D. V. Patil, Physica A **392**, 2701 (2013).
[34] D. Galant, Math. Comput. **23**, 674 (1969).
[35] B. Shizgal, J. Comput. Phys. **41**, 309 (1981).
[36] Y. Sone, S. Takata, and T. Ohwada, Eur. J. Mech. B-Fluids **9**, 273 (1990).
[37] U. Ghia, K. N. Ghia, and C. T. Shin, J. Comput. Phys. **48**, 387 (1982).
[38] P. Bahukudumbi, J. H. Park, and A. Beskok, Microscale Thermophys. Eng. **7**, 291 (2003).
[39] J. Fan and C. Shen, J. Comput. Phys. **167**, 393 (2001).
[40] B. John, X.-J. Gu, and D. R. Emerson, Numer. Heat Transfer, Part B **58**, 287 (2010).
[41] B. John, X. J. Gu, and D. R. Emerson, Comput. Fluids **45**, 197 (2011).
[42] A. Mohammadzadeh, E. Roohi, and H. Niazmand, Numer. Heat Transfer, Part A **63**, 305 (2013).
[43] S. Naris and D. Valougeorgis, Phys. Fluids **17**, 097106 (2005).
[44] S. Varoutis, D. Valougeorgis, and F. Sharipov, J. Comput. Phys. **227**, 6272 (2008).
[45] S. Mizzi, D. R. Emerson, S. K. Stefanov *et al.*, J. Comput. Theor. Nanosci. **4**, 817 (2007).
[46] A. Rana, M. Torrilhon, and H. Struchtrup, J. Comput. Phys. **236**, 169 (2013).